Title

Complex dislocation loop networks as natural extensions of the sink efficiency of saturated grain boundaries in irradiated metals.

Journal

Science Advances, 10(18)

Authors

He, Sicong
Mang, Emily
Leff, Asher
et al.

Publication Date

2024-05-03

DOI

10.1126/sciadv.adj8395

Peer reviewed

MATERIALS SCIENCE

Complex dislocation loop networks as natural extensions of the sink efficiency of saturated grain boundaries in irradiated metals

Sicong He[1], Emily H. Mang[2], Asher C. Leff[3]†, Xinran Zhou[1], Mitra L. Taheri[2], Jaime Marian[1]*

The development of radiation-tolerant structural materials is an essential element for the success of advanced nuclear energy concepts. A proven strategy to increase radiation resistance is to create microstructures with a high density of internal defect sinks, such as grain boundaries (GBs). However, as GBs absorb defects, they undergo internal transformations that limit their ability to capture defects indefinitely. Here, we show that, as the sink efficiency of GBs becomes exhausted with increasing irradiation dose, networks of irradiation loops form in the vicinity of saturated or near-saturated GB, maintaining and even increasing their capacity to continue absorbing defects. The formation of these networks fundamentally changes the driving force for defect absorption at GB, from "chemical" to "elastic." Using thermally-activated dislocation dynamics simulations, we show that these networks are consistent with experimental measurements of defect densities near GB. Our results point to these networks as a natural continuation of the GB once they exhaust their internal defect absorption capacity.

INTRODUCTION

Materials containing a large internal surface-to-volume ratio are important in many technologically important areas of science, including catalysis (*1*–*3*), mechanical strength (*4*), magnetism (*5*), or corrosion (*6*–*8*). In irradiated materials, grain boundaries (GBs) can act as effective sinks for defects, potentially resulting in an enhanced radiation resistance compared to their single-crystal counterparts (*9*–*15*). The best experimentally quantifiable indicator of GB sink efficiency has been the width of defect-free areas adjacent to interfaces known as defect denuded zones (DZs). DZs are the microstructural manifestation of highly complex defect-GB interactions. Broadly speaking, these interactions relate the overall GB character, defined by the five-dimensional (5D) space consisting of misorientation and inclination degrees of freedom (dof), with the structure and properties of irradiation defect clusters, although extensive studies in recent times culminating in previously unidentified findings and a much improved understanding of the internal structure of GBs are fast changing this picture (*6*, *16*–*19*). In a previous work (*20*), we have shown that the evolution of the width of the DZ with irradiation dose is associated with changes in GB (internal) microstates. Transitions between different allowable GB microstates occur because of alterations in the atomic structure of GB due to absorption of irradiation defects. Such transitions are governed by a spectrum of time relaxation constants that reflect the hierarchy of microstate free energies and its partition function. Together, they set the interplay between irradiation dose rate and internal GB changes, leading to evolution equations that predict the time behavior of the DZ (*21*). In other words, under irradiation, certain GBs exhibit DZ collapse without altering their overall macroscopic dof, i.e., these changes are solely navigated by internal transformations at the level of GB microstates.

[1]Department of Materials Science and Engineering, University of California Los Angeles, Los Angeles, CA 90095, USA. [2]Department of Materials Science and Engineering, Johns Hopkins University, Baltimore, MD 21218, USA. [3]Army Research Laboratory, Adelphi, MD 20783, USA.
*Corresponding author. Email: jmarian@g.ucla.edu
†Present address: TauMat LLC, 10010 Portland Pl., Silver Spring, MD 20901, USA.

However, while the macroscopic descriptors of the GB are seen to remain unchanged, Nye tensor analysis performed on these GBs reveals that DZ collapse manifests itself as an accumulation of geometrically necessary dislocations (GNDs) in the region previously occupied by the DZ itself. GND accumulation is typically interpreted as resulting from lattice curvature changes associated with the emergence of a dislocation substructure with an unbalanced Burgers vector. A problem immediately arises when trying to reconcile the observation of GND with the known fact that the only source of dislocation content in irradiated metals is the production of small, perfect prismatic loops originating within displacement cascades (*22*–*24*). By themselves, these loops contribute no net GND density in a global sense (i.e., when the Nye tensor is calculated along the entire loop contour in a single sweep), and, thus, the puzzle of how they form remains. Moreover, how these GNDs are connected to DZ suppression is also lacking a proper physical explanation.

In a previous paper, we have shown that caution must be used when reconciling experimental GND footprints with a formal definition of the Nye tensor (*25*). For one, we have shown that GND intensities are strongly dependent on the resolution of the discretization used. This is crucially important when comparing simulated images with experimental signals extracted using a fixed spatial resolution. Trivially, the loop size sets the threshold discretization limit under which calculated GND densities deviate from the continuum definition of the Nye tensor. Ideally then, the experimental resolution should be tailored to the defect sizes expected under the particular irradiation conditions, which is of course highly impractical. Another aspect worth mentioning when comparing simulations and experiments is that pixelated Nye tensor images obtained under the microscope are eminently 2D, which projects 3D features onto the imaging plane with the consequent loss of configurational information.

The above issues relate to the handling of microscopic experimental information and its relationship to the numerical aspects of the Nye tensor determination. They do not address, however, the physics gap separating the emergence of a GND footprint with the collapse of the DZ in irradiated materials. The main objective of the present paper is to provide a physical picture that reconciles experimental GND density measurements, notional definitions of the Nye

tensor, and a connection between microstructural evolution under irradiation and changes in the microstates of a GB. Our model is based on the presumption that a dislocation network emerges in the GB-adjacent region during irradiation as the GB defect absorption efficiency evolves toward saturation. We consider this dislocation network to be a main component of the sink efficiency, which thus must be taken into account in our consideration of the role played by GBs during irradiation. Our work provides potential channels to control sink strength by tailoring these GB-adjacent regions, which could have a marked impact on the effectiveness of optimizing radiation tolerance using techniques such as GB engineering.

The paper is organized as follows. First, we present the physical hypotheses behind the formation of imbalanced GND networks forming as a consequence of GB sink efficiency loss and the accumulation of small irradiation loops. Second, we introduce the experimental observations and the techniques used to extract and interpret quantitative information from them. We then describe the numerical methods used to generate Nye tensor signals and discuss the main simulation parameters. We subsequently show that dislocation networks of the type hypothesized earlier are a natural manifestation of the irradiation damage microstructure during the loss of defect absorption efficiency by GBs. This is followed by a comparison between the Nye tensor signals emerging from these networks and experimental signals, providing the basis for validation of our mechanistic hypotheses and a confirmation of the physical interpretation of the experimental images. We finalize with a discussion of the results and our most important conclusions.

MECHANISM OF NETWORK FORMATION NEAR SATURATED GBS UNDER IRRADIATION

A closed dislocation loop of any character yields no net GND signal. This is readily seen from the mathematical definition of the Nye tensor, $\boldsymbol{\alpha}$

$$\boldsymbol{\alpha} = \frac{1}{V}\oint \mathbf{b} \otimes d\mathbf{l} \tag{1}$$

where V is the system volume, $\mathbf{b}$ is the Burgers vector, and $d\mathbf{l}$ is an infinitesimal length vector that runs along the loop's geometric contour and that is usually expressed as a normalized vector so that $\boldsymbol{\alpha}$ can directly represent a dislocation density. For convenience, it is common to use scalar values of the Nye tensor by working with the norms $\|\boldsymbol{\alpha}\|_1$ or $\|\boldsymbol{\alpha}\|_\infty$.

From Eq. 1, a nonzero $\boldsymbol{\alpha}$ implies the existence of a Burgers vector imbalance that is incompatible with a closed loop. However, the notion of a net nonzero GND signal originating from irradiation defects consisting exclusively of closed prismatic loops can be reconciled considering the following two processes:

The first one involves the incomplete absorption of prismatic loops, either as a consequence of GB saturation or due to a topological incompatibility between a loop's Burgers (lattice) vector and admissible displacement-shift complete (DSC) vectors (*25*).

The second involves processes such as that presented in Fig. 1, which shows a schematic diagram of the reaction between two $^1/_2\langle 111\rangle$ prismatic dislocation loops gliding in their respective glide cylinders (shown as quadrangular prisms for simplicity). This is consistent with motion by 1D random walk typical of small prismatic loops generated in displacement cascades (*26*, *27*). In isolation, each of these loops contributes zero Nye tensor signal. However, the two loops eventually enter the coincident glide volume (shown as a shaded orange cube) and react according to the dislocation reaction

$$\frac{1}{2}[111] + \frac{1}{2}[1\overline{1}\overline{1}] \rightarrow [100] \tag{2}$$

which is an exothermic reaction according to Frank's rule (*28*). As a result, a [100] segment is created, shown in black in Fig. 1. Specifically, in α-Fe, ⟨100⟩ segments have very high migration energies and turn otherwise highly mobile $^1/_2\langle 111\rangle$ loops into sessile, i.e., immobile, structures (*29*–*31*). Crucially, the ⟨100⟩ segment is now unbalanced, and it then may contribute a net GND signal when the spatial discretization over which such signal is analyzed has a similar size as the original loops. This can be seen in Fig. 2A, where the simulated GND footprint of two hexagonal $^1/_2\langle 111\rangle$ prismatic loops in 2D is shown both when they are separated by some distance and also when they react forming a ⟨100⟩ segment. It is clear that, in isolation, the loops do not produce a significant footprint (the weak signal appreciated in the figure is due to the use of a scalar norm, which provides a numerical value even for a nominal zero footprint), whereas an intense signal is detected for the unbalanced ⟨100⟩ segment. However, for discretizations larger than the whole reacted structure, the net GND signal still adds up to zero for a closed loop. See mesh size analysis in (*28*).

The above two processes are not mutually exclusive and constitute the elemental mechanisms by which a "network" composed of $^1/_2\langle 111\rangle$ and ⟨100⟩ segments can form by the sustained arrival of irradiation loops to a saturated GB. The mechanism then proceeds through a series of sequential steps, described in the following:

1. Once the GB is no longer able to absorb the incoming defects at the speed dictated by the irradiation dose rate, self-interstitial

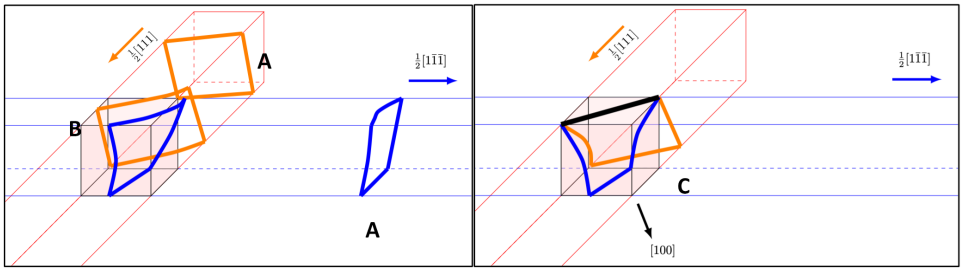

Fig. 1. Mobile prismatic loops react and turn into sessile structures. Schematic sequence of two square $^1/_2\langle 111\rangle$ prismatic dislocation loops (orange and blue) (**A**) gliding along their glide prisms (delineated by the thin orange and blue lines) on a collision trajectory; (**B**) coming into contact within the reaction volume (shaded cube); and (**C**) reacting to form a [100] junction along their common intersection. The process is driven by elasticity and unidimensional random diffusion (1D Brownian motion). The junction (black segment) is unbalanced and satisfies the Burgers vector reaction $\frac{1}{2}[111] + \frac{1}{2}[1\overline{1}\overline{1}] \rightarrow [100]$.

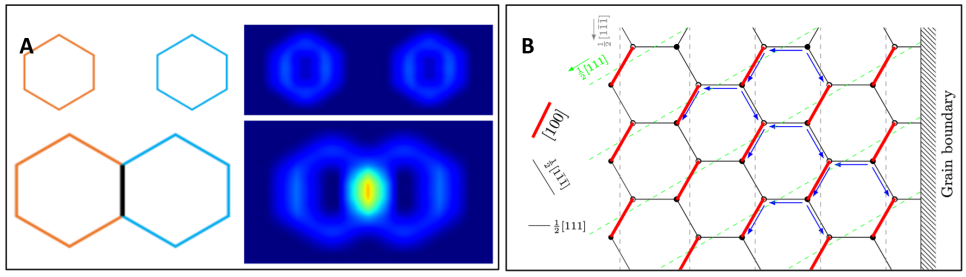

Fig. 2. Dislocation loops can be imaged as diffuse maps of their GND intensity. (**A**) Simulated GND footprints of two hexagonal $^1/_2\langle 111\rangle$ prismatic loops when (top) they are separated beyond their reaction distance and (bottom) after reaction along one of their edges (color map in arbitrary units). Color coding: red, $\frac{1}{2}[\bar{1}11]$; blue, $\frac{1}{2}[\bar{1}\bar{1}\bar{1}]$; and black, $[\bar{1}00]$. (**B**) Schematic representation of an idealized prismatic loop network composed of $\langle 111\rangle$ and $\langle 100\rangle$ segments forming from a saturated GB (located on the right edge of the image).

atom (SIA) loops become only partially absorbed. This leads to a population of "half"-loops on top of the GB plane. This is illustrated by the segments that directly abut to the GB in Fig. 2B (right-hand side of the image).

2. Subsequent migration of prismatic loops results in segment-segment interactions near the GB. Occasionally, some of those interactions result in reactions of the type shown in Fig. 1 and Eq. 2. With time, a network consisting of $^1/_2\langle 111\rangle$ and $\langle 100\rangle$ segments starts to form adjacent to the GB.

3. Several layers of reactions lead to the buildup of a network against the saturated GB. An idealized representation of this network is shown in Fig. 2B, where all four $^1/_2\langle 111\rangle$ Burgers vectors of the body-centered cubic (bcc) lattice are indicated.

In reality, actual networks are not ideal and consist instead of irregular configurations of dislocation segments, some looking like coalesced loops, some containing $\langle 100\rangle$ junctions, generally arranged spatially in a heterogeneous manner. Note that, once a GB has saturated its capacity to absorb damage, the main driving force for the arrival of prismatic loops to the GB is the elastic energy reduction associated with the reaction shown in Eq. 2 (which results in a 33% reduction in elastic energy). In addition, it is worth noting that, while the present analysis does not require that the nature of the loops, i.e., whether they are of SIA or vacancy type, be specified, it is known that, in cubic crystals, the vast majority of prismatic loops created are of SIA type, transitioning from 3D to 1D migration paths above a critical loop size (*32*, *33*).

Next, we carry out detailed simulations of the mechanism just presented under constraints designed to mimic experimental conditions and obtain their corresponding Nye tensor representation. The network structure depends, among others, on the diffusion behavior of the loops (set by the temperature), their relative trajectories (set by the crystal structure), mutual elastic interactions (set by the loop sizes and shapes), and their production rate (primarily set by the irradiation particle energy and dose rate). These relaxed networks give rise to Nye tensor fingerprints that can then be directly compared with experiments specifically performed to enable such evaluations.

METHODS

Experimental

Film preparation, irradiation, and characterization

Nanocrystalline iron thin films were deposited via balanced dc magnetron sputtering using a 99.9% pure Fe target onto polished substrates of NaCl (100) single-crystal substrates and prepared as detailed by Vetterick *et al.* (*34*). The resulting thin films had a nominal thickness of 100 to 150 nm. In preparation for thin-film liftouts, cleaved thin-film samples were prepared by floating off and bonding films onto 200-mesh transmission electron microscopy (TEM) grids. Liftouts of columnar, polycrystalline Fe film were generated using a focused ion beam, and cross sections were characterized using a 200-kV JEOL 2100 LaB6 TEM at Sandia National Laboratories. The samples were irradiated using 10-keV He^+ ions with a 10-kV Colutron source at a dose of 3.7×10^{-3} displacements per atom (dpa) per second and a temperature of 573 K (*35*, *36*). As explained in these and other studies, a large proportion of the implanted He ions is likely to bind itself to vacancies of their own creation (*37*) or created by recoils, thus immobilizing and disconnecting them from further evolution. As well, while He is injected in sufficient quantities to form bubbles in the corresponding depth range, these bubbles have limited mobility even at 573 K and are thus not expected to participate directly in the dynamics of loop network formation near GBs (*20*).

Bright-field TEM images acquired during in situ irradiation were collected at a constant two-beam diffraction condition, and in situ irradiation videos were captured at a frame rate of 30 frames per second. However, it should be noted that bright-field TEM does not provide sufficient spatial resolution to capture structural information. For that reason, intermittent precession electron diffraction (PED)–automated crystallographic orientation mapping (ACOM) was conducted throughout irradiation at doses of 0.0, 6.1, 12.2, and 18.3 dpa to demonstrate structural evolution with respect to dose (*38*, *39*). PED-ACOM data were used for GND density calculation inputs (*40*).

GB structure and experimental Nye tensor analysis

GND signals are observed via mapping of lattice curvature gradients according to

$$\boldsymbol{\alpha} = \kappa^T - \mathrm{Tr}(\boldsymbol{\kappa})\boldsymbol{I} \tag{3}$$

which is known as Nye's equation, linking the curvature gradient tensor $\boldsymbol{\kappa}$ to the GND tensor (*40*–*42*). The components κ_{ij} are obtained as the local gradient of the lattice orientation map, i.e., $\kappa_{ij} = \partial\omega_i/\partial x_j$, where ω is the lattice orientation vector, which is, in turn, obtained from discrete pixelations of spatially resolved PED-ACOM data. A scalar metric of the GND density ($\|\boldsymbol{\alpha}\|_1$ in our case) is then used for graphical representation (*25*).

Computational models

Physics modeling of irradiation loop dynamics

The computational methodology developed in this work is designed to capture irradiation loop diffusion and elastic interactions, including

self-interactions (i.e., between segments belonging to the same loop) and loop-loop interactions (between segments belonging to different loops). Diffusion is modeled following the physical mechanism ascribed to prismatic loops generated in displacement cascades, namely, 1D diffusion along the Burgers vector direction. The diffusivity for one such loop is inversely proportional to the loop size, given by the expression (*33*)

$$D(T,\boldsymbol{\sigma};n) = D_0(n)\exp\left[-\frac{\Delta Q(\boldsymbol{\sigma})}{kT}\right] \quad (4)$$

where T is the absolute temperature, $\boldsymbol{\sigma}$ is the stress tensor at the position of the loop, and n is the number of SIA in the loop. $D_0(n)= 8.98\times10^{-3}n^{-0.61}$ (in square centimeters per second) is a diffusion pre-factor that captures the defect size dependence of the loop diffusivity and $\Delta Q(\boldsymbol{\sigma})$ is an activation energy that depends on the local stress state. $\boldsymbol{\sigma}$ is obtained within a non-singular linear elasticity framework implemented in a dislocation dynamics (DD) code. $\Delta Q(\boldsymbol{\sigma})$ comprises a crystallographic contribution, ΔE_m, associated with migration along the prismatic coordinate, and an elastic contribution, $\Delta W_{\mathrm{el}}(\boldsymbol{\sigma})$, associated with the work done by the elastic forces during loop glide

$$\Delta Q(\boldsymbol{\sigma}) = \Delta E_m - \Delta W_{\mathrm{el}}(\boldsymbol{\sigma}) = \Delta E_m - \boldsymbol{f}_{\mathrm{el}}\mathbf{b}L \quad (5)$$

where $\mathbf{b}$ is the Burgers vector and $\boldsymbol{f}_{\mathrm{el}}$ is total elastic force on a segment of length L. In DD methods, $\boldsymbol{f}_{\mathrm{el}}$ is obtained as the linear superposition of the Peach-Köhler force originating from all other segments in the simulation cell, i.e., $\boldsymbol{f}_{\mathrm{el}} = \sum_i \boldsymbol{\sigma}_i(\mathbf{b}\times\boldsymbol{t})$, where the subindex i runs over all dislocation segments, each with its own line direction $\boldsymbol{t}$ (*43*). With this, the loop dynamics is controlled by the following set of equations:

$$\mathbf{v} = \boldsymbol{M}\boldsymbol{f}_{el} \quad (6)$$

$$\delta x = v\delta t \pm \xi\sqrt{2D\delta t} \quad (7)$$

where $\boldsymbol{M}$ is the dislocation mobility tensor (further explanation about $\boldsymbol{M}$ is given in the Supplementary Materials), $\mathbf{v}$ is the velocity vector ($v = \|\mathbf{v}\|$ is its modulus), ξ is a uniform random number between 0 and 1, and δt is the timestep. The segment displacement, δx, is thus a combination of a "mechanical" contribution and a "thermal" or diffusive one. Note that the diffusive contribution is treated here as a stochastic (Wiener) process and thus can be in the direction of or against the elastic forces (as represented by the "±" symbol in the equation). Moreover, for a closed prismatic loop, the shear stresses have the effect of torquing the loop, which induces no net displacement. As such, defect migration is controlled by the thermal component until segment-segment collisions take over as the dominant process.

Calculation and processing of GND fingerprints

The relaxed network configurations are processed with GND fingerprint parsers developed by the authors (*25*). First, the simulation volume containing the network is discretized by tessellating it with the desired spatial resolution. The parser then identifies the intersections between mesh cells and dislocation loops and places nodes at the intersection sites on the cell boundaries. The GND density is then calculated in each cell according to Eq. 1, and the resulting cell densities are processed using the Plotly library (*44*) to generate 3D color maps with a prescribed signal intensity spread.

RESULTS

Experimental GND maps as a function of irradiation dose

Figure 3 shows the change in GND density with dose of four distinct grains in the irradiated material (illustrated in rows A to D in the figure). The microstructure is seen to undergo a highly heterogeneous temporal and spatial GND density evolution, with clear distinctions depending on the grain matrix observed. The most salient features that can be reasonably extracted from the observations are as follows:

1. As shown in all figures, different GBs behave differently, even in adjacent GBs belonging to the same grain.

2. Figure 3 (A and C) reveals a gradual transfer with increasing irradiation dose of GND density from the grain interior toward the GB.

3. Figure 3 (B and C) displays the existence of twin boundaries, captured as elongated high-GND intensity planes.

4. Strong redistributions of GND content can be appreciated in Fig. 3B. GNDs appear to concentrate first near GBs and in selected locations inside the grain (possibly along native dislocation lines), subsequently accumulating in half of the grain volume, depleting the other half to practically zero GND concentration.

5. None of the native GBs is seen to displace or suffer any transformation that suggests changes in GB macrostates.

Next, we present simulation results designed to put our network formation hypothesis to the test and add insight to the experimental observations.

Simulation results

To carry out the simulations, we construct a computation cell with dimensions of 20 by 20 by 20 nm, with the GB being one of the external edges of the computational cell and periodic boundary conditions in the two directions parallel to the GB. The GB normal corresponds to the crystallographic direction [012] of the computational cell's crystal lattice, representing a $\boldsymbol{\Sigma}5$ boundary with 53.1° misorientation. Loops are generated at a distance of 20 nm from the GB at a random location relative to the 2D GB plane. The Burgers vector is assigned at random among the four ⟨111⟩-independent directions in the bcc crystal lattice. The loops all have hexagonal shape and have a size (hexagon width) ranging between 2.5 and 5.0 nm, sampled uniformly. This mimics reasonably well the defect shapes and size distributions observed in most studies of Fe irradiation (*45*, *46*). Using the GB area and the number of loops entering the simulation cell, we correlate loop densities to irradiation dose.

Formation and evolution of the dislocation loop network

We start with a pristine planar GB assumed to be in a saturated state, i.e., unable to fully absorb incoming defect loops. Instead, loops become partially absorbed, giving rise to substructures such as that shown in Fig. 4A. After a certain irradiation dose, these substructures "blanket" the GB, leaving no exposed surface for subsequent loops to directly interact with the boundary (Fig. 4B). The next loop interacts instead with one or several of the partially absorbed loops, as shown in Fig. 4C. This interaction is spatially complex, as it is governed by elasticity in 3D and loops of various sizes and orientations. Here is where the DD module becomes critical, to capture long-range elastic interactions and apply short-range inelastic interaction rules (segment-segment reactions). After considering several hundred loop arrivals corresponding to an approximate a total dose of 1.0 dpa (the estimation of the dose in the DD simulations is explained in section S.3), a network is formed in the near-GB region, as shown in Fig. 4D.

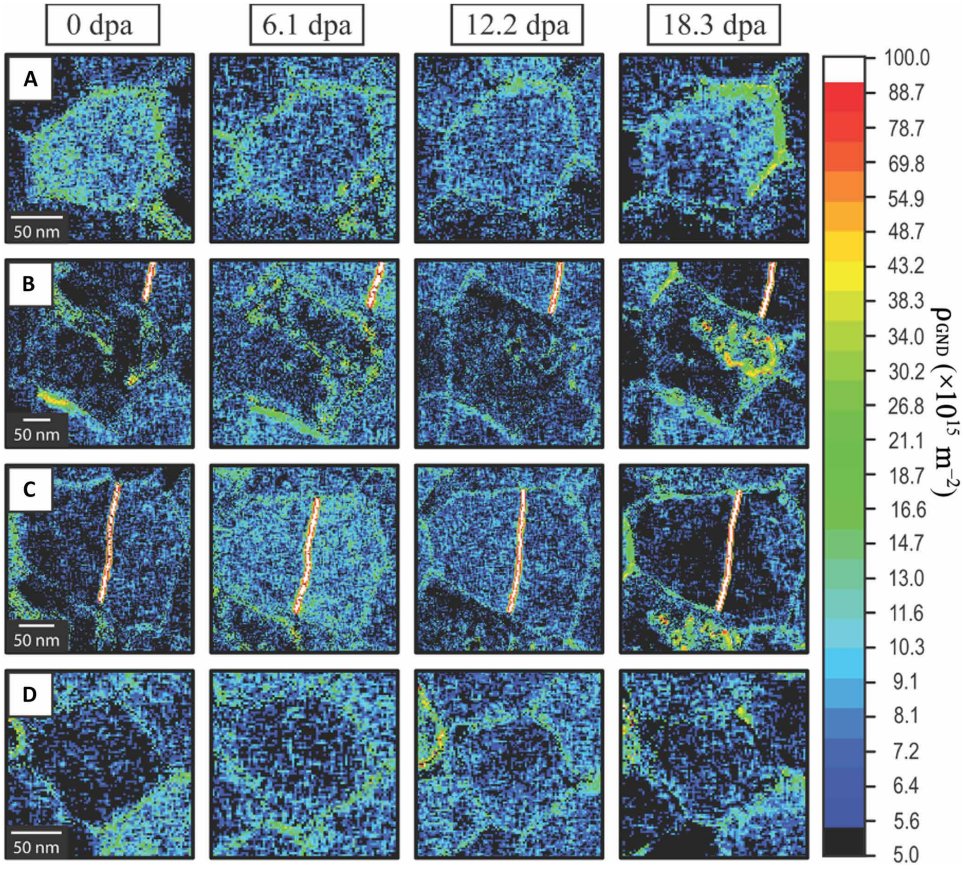

Fig. 3. Irradiation of nanocrystals produces inhomogeneous accumulation of crystal defects. Nye dislocation tensor maps generated from PED ACOM orientation data, highlighting the increase of GND density at the GBs, as well as the evolution of Nye tensor signals, proposed to be dislocation networks, throughout differing nanocrystalline grain matrices (**A** to **D**) with the increase in He ion damage from 0.0 to 18.3 dpa.

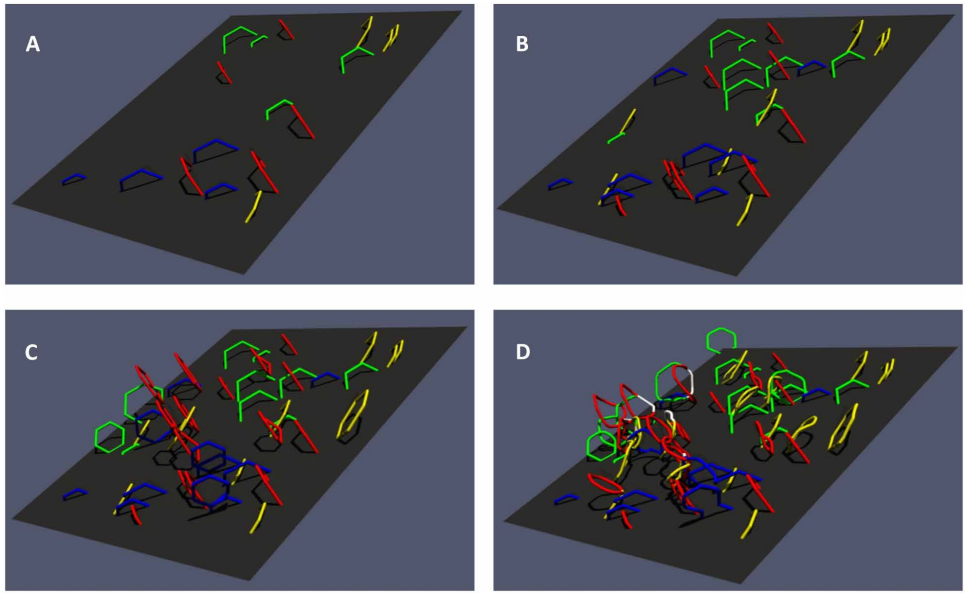

Fig. 4. Simulations of defect absorption at GBs reveal the formation of a loop network. (**A**) Initial formation of partial loop substructures on a saturated GB. The loops are colored according to their Burgers vectors. (**B**) The GB is fully "blanketed" by partial loops. (**C**) Snapshot showing the arrival of the first loop that does not reach the GB (interacting instead with the half-loops). (**D**) Final loop network after 1.0 dpa of irradiation. Color coding: red, $\frac{1}{2}[11\bar{1}]$; yellow, $\frac{1}{2}[\bar{1}11]$; green, $\frac{1}{2}[1\bar{1}1]$; blue, $\frac{1}{2}[\bar{1}\bar{1}1]$; and white, ⟨100⟩.

This network displays several interesting features. The main outcome of loop-loop interactions in the near-GB region is (i) coalescence of two loops with the same Burgers vector and (ii) the formation of ⟨100⟩ segments from reactions between loops with dissimilar ones. Both of these can be appreciated in Fig. 4D (⟨100⟩ junctions shown in white). The conditions for prismatic loop coalescence have been studied in detail by McElfresh *et al.* (*47*, *48*) and are also briefly discussed in section S.2. We have simulated 10 independent configurations with the same conditions as those in Fig. 4, all with similar qualitative outcome (see section S.3 for more examples). For statistical significance, we also have simulated 60 nm–by–60 nm GB plane configurations, which we use to generate GND fingerprint images in the next subsection.

GND analysis

Figure 5 shows a color map of a loop network configuration relaxed over a GB plane with dimensions of 60 nm by 60 nm. The image is then processed according to the procedure described in the "Calculation and processing of GND fingerprints" section using a pixel resolution of 10 nm and a spread of 5 nm. Note that this is consistent with the experimental resolution of 10 to 12 nm used in the studies referenced earlier (*36*, *39*) and appropriate to avoid any analysis artifacts related to the spatial discretization, i.e., sufficiently coarse to not produce a net GND signal for individual loops but fine enough to detect segments with unbalanced Burgers vectors due to loop reactions. Figure 5 shows two views: one directly edge-on to the GB plane and another tilted by 30° for oblique view. The color map has been chosen to capture the range of GND densities measured in the experiments (using the same color palette for ease of comparison). Our analysis thus confirms that irradiation loop networks can furnish GND fingerprints detectable through lattice curvature measurements with nanometer resolution.

As well, it is of interest to analyze the intense GND bands traversing the grains in Fig. 3 (B and C). Our starting hypothesis is that these correspond to preexisting low-Σ boundaries (e.g., Σ3 or Σ5) created during processing prior to irradiation. Taking as an example the configuration contained in the area indicated by the dashed line in Fig. 3C, we carry out an analysis of the GND density assuming that it corresponds to a thin twin plate bounded by two 109° ⟨110⟩ Σ3 twin boundaries. The results are shown in Fig. 6, where the associated lattice orientation component along the ⟨110⟩ direction is shown along with its gradient, the lattice curvature. As shown, the GND fingerprints corresponding to this configuration display are characterized by dislocation densities that are one order of magnitude larger than those shown in Fig. 5. A similar analysis performed for a ≈37° ⟨100⟩ Σ5 boundary led to identical results, thus confirming the nature of the structure shown in the inset of the figure. Next, we discuss the most important aspects of our results and the implications for the interpretation of microstructural evolution in irradiated nanocrystalline materials.

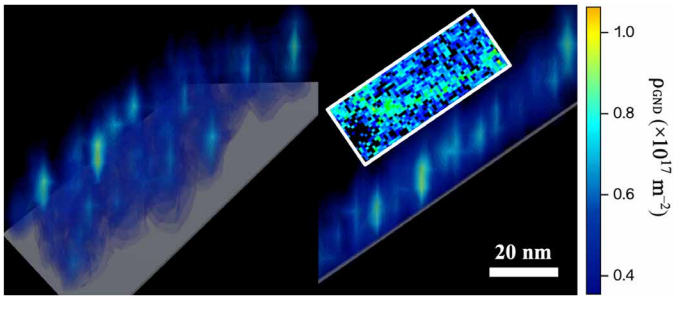

Fig. 5. Comparison between simulations and experiments leads to identification of key mechanisms. Rendition of the configuration shown in Fig. 3B processed as explained in the "Calculation and processing of GND fingerprints" section. The left image is a side view (edge-on to the GB), whereas the one on the right is the same configuration tilted at an angle. The inset corresponds to the box highlighted in Fig. 3A. The color bar for the GND density is quantitatively equivalent in both cases.

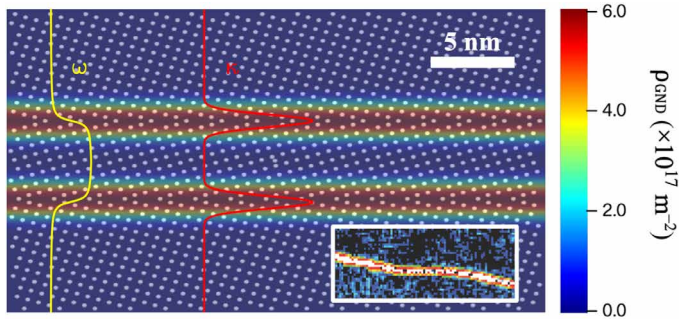

Fig. 6. Atomistic simulations reveal defect structures. Calculated GND fingerprint of a twin plate bounded by two Σ3 boundaries (≈109°-misorientation GB), showing the underlying atomistic structure seen along a ⟨110⟩ crystal direction. Superimposed on the image are the profiles for the lattice orientation ω and the lattice curvature κ profiles. The inset corresponds to the box highlighted in Fig. 3C.

DISCUSSION

The present paper incorporates two original contributions that are worth discussing in more detail. First, we introduce a hypothesis explaining the reasons behind the emergence of strong GND fingerprints with irradiation dose near GBs. This hypothesis is then tested using advanced models for defect transport and evolution. Second, we provide a quantitative comparison of simulated/calculated GND fingerprints with experimental images, with considerable agreement achieved between both approaches.

Phenomenology of DZ evolution near GBs in irradiated crystals

Structural materials for advanced nuclear energy concepts (e.g., fusion energy) will have to contend, among other things, with unprecedented levels of irradiation dose. Materials will not be capable of withstanding these high doses unless the concomitant irradiation damage defects are removed, to a large degree, as they are being produced. GBs have long thought to be effective defect sinks, which has brought nanocrystalline materials to the forefront of radiation-tolerant material design strategies. However, GBs are not ideal sinks, at least not permanently, and their efficacy in removing irradiation defects must be carefully studied. DZ formation and "collapse" is seen as a strong marker of GB defect absorption efficiency, as its existence, or lack of, can be directly mapped to defect concentration profiles near GBs that are directly influenced by their sink strength. Previous work has established a clear connection between this sink efficiency and the macroscopic GB character (*16*, *49*), as well as between sink efficiency and DZ formation (*35*, *50*–*54*). However, we have recently demonstrated that changes in absorption efficiency can lead to DZ collapse without the need for a change in macroscopic GB dof (*20*).

Our work has also shown that changes in irradiation defect concentration can be mapped to changes in the GND density. However, interpreting these GND signals in the context of irradiation damage production was not clear, as defects are universally produced as small, closed loops that should, in principle, contribute no net Nye tensor fingerprints. The work presented here attempts to provide the link that explains the equivalence between observed GND fingerprints and what we know about damage production. We prove that networks of damage loops can be shown to produce nonzero Nye tensor signals. The preconditions for these networks to form are as follows:

1. DZ collapse must have occurred as a prior condition. This means that the GB may have run through its entire hierarchy of available microstates, exhausting its ability to accommodate defects via changes in its internal dof.

2. Subsequently, the exposed surface of the saturated GB must undergo a partial coverage with semi-absorbed loops (Fig. 4B). This process is likely to be the rate-limiting step in the entire process.

3. The material in question must allow reactions among damage loops that change the balance of Burgers vector along the loops' perimeters. Mathematically, this amounts to a closure failure of the integral in Eq. 1. In the present case, such reactions are represented by Eq. 2.

4. The formation of these networks immobilizes defects near the GB region, resulting in a gradual transfer of matter from the grain's interior toward the GB. The kinetics of the process switches from being driven by chemical forces (concentration gradients) to mechanical ones (elastic forces). This represents a partial paradigm change, as it is the network now, instead of the GB per se, that acts as the sink for defects going forward in time.

Discussion on simulation methods and comparison with experimental results

While DD models have been extensively used to simulate dislocation loop dynamics, our model adds two original elements that are worth discussing. First, it captures loop reactions of the type described by Eq. 2, which gives rise to experimentally observed ⟨100⟩ segments typical of irradiated Fe microstructures. Second, it simulates a (semi-) saturated GB as a planar boundary with partially absorbed, immobile, prismatic loops. This is based on molecular dynamics simulations of prismatic loop interactions with a Σ5 boundary (*25*). Our model also captures all four independent $^1/_2\langle 111\rangle$ Burgers vectors of the bcc crystal lattice, which thus sets no geometric limitations on the space of dislocation reactions among different irradiation loops.

In terms of comparison, as Fig. 5 shows, the color map of the GND fingerprints in the simulated structures and the experimental images are in good agreement in regard to the accumulated GND densities. Although GND fingerprints are a scalar integrated quantity where much of the fine details of the microstructure are lost, this confirms (i) that the loop sizes, shapes, densities, and network structure considered in the models are consistent with the experimentally revealed structures, and (ii) the correspondence between the physical manifestation of the Nye tensor according to its two definitions, Eqs. 1 and 3, i.e., the equivalence between the dislocation-based definition used in the DD model and the one based on lattice curvature gradients considered in the experiments.

In real specimens, which are thin TEM discs with thicknesses on the order of 150 nm, surface sinks will compete with GBs for mobile loops (*55*) likely delaying the onset or formation of the absorbing loop network near GBs relative to bulk specimens such as those nominally represented by the simulations. A proper treatment of the effect of the free surfaces on the timescale of network formation requires a more detailed computational analysis where the geometry of the TEM discs is explicitly considered, but this is presently beyond the scope of this work. For this reason, however, the comparison between the observed doses at which the network forms in experiments and simulations should be done with caution.

Consistency of the present results with radiation damage theories

Defects are produced in displacement cascades in numbers and sizes that vary across material class, particle type and energy, temperature, and existing microstructure. Thanks to several decades of research combining detailed electron microscopy and atomistic simulations, we now have a deep understanding of the structure and numbers of these irradiation defects. Although we cannot ascertain from images such as those shown in Fig. 3 what the nature of the observed defect is, we can confidently infer that they are of SIA type. It is known that, in cubic metals, the large mobility difference between SIA and vacancy defects (up to several orders of magnitude depending on temperature) tilts the balance toward a preferential arrival of self-interstitial clusters at defect sinks. Moreover, SIA clusters move along rectilinear paths, covering much longer distances than vacancy defects in the same amount of time. Such features form the basis of one of the pillars on which irradiation damage theory rests: the so-called production bias (PB) model. The PB model is captured in our simulations, and the relatively good agreement between the simulated and experimental GND fingerprints, both qualitative and quantitative (referred to the total GND densities), is an indirect confirmation of the partial validity of our assumptions as it relates to prismatic loop sizes and shapes.

In terms of the role played by vacancies, while the temperature at which the irradiations were carried out (573 K) is well above the stage III temperature in Fe [≈200 K (*56*), at which monovacancies become mobile], it is worth remarking that the injection of He ions during implantation has the immediate effect of immobilizing monovacancies and vacancy clusters, allowing self-interstitial clusters to escape the cascade region and favor their accumulation near the GB without a delayed recombination effect. This is likely to facilitate the formation of loop networks with strong GND signals, as vacancies remain trapped by He atoms in the interior of the grain or are released in negligible concentrations, not sufficient to affect the formation of the network. This mechanism is expected to hold up to the peak swelling temperature, which for Fe is ~700 K (*57*). At temperatures beyond that, the bubbles begin to dissolve by evaporation of vacancies and desorption of the He atoms, which could conceivably lead to delayed recombination and the dissolution or weakening of the SIA loop network.

The other pillar, referred to as the dislocation bias model, refers to the preferential absorption of SIA clusters by defect sinks. Once again, our models are consistent with this picture, taking a saturated GB, i.e., one that has exhausted its ability to absorb more damage loops, as the starting configuration for our simulations. From this, an interesting picture emerges, wherein, as a GB exhausts its capacity to absorb damage loops, the system ascribes a strip of material immediately adjacent to the GB to continue storing defects. In other words, the effective thickness of the GB widens as to maintain a high sink efficiency overall. This could be a natural mechanism to keep absorbing damage when the actual GB has become saturated. This is

reminiscent of the notion of complexions in deformed nanocrystalline systems (*58*–60), which act as extensors of the disordered region of a GB beyond the strict interface separating two grains with dissimilar orientations.

Closing thoughts

We have developed a discrete DD model that incorporates thermal motion of dislocation loops to simulate loop network formation and evolution near GBs in irradiated Fe. The model successfully predicts the formation of a prismatic dislocation loop network near a saturated GB. The network is stabilized by energy-reducing dislocation-dislocation interactions such as coalescence and the formation of ⟨100⟩ junctions.

We have processed the complex dislocation loop network structure with software that extracts and images its GND content, enabling direct comparison with Nye tensor analysis of experimental lattice curvature observations using PED. We find a remarkable agreement between the GND fingerprints generated by the simulated network and those measured experimentally.

We find that loop networks can maintain a high defect sink efficiency once the actual GB has become saturated, switching the absorption mode from being concentration-driven to elastically driven. The network thus acts as a functional extension of the GB as a defect sink once the latter have exhausted its ability to absorb damage.

One of the implications of our findings is that the collapse of the DZ does not necessarily imply an inability for self-healing in irradiated materials. In systems that favor (or enable) the formation of loop networks, a high sink efficiency can be maintained even after DZ collapse, maintaining the material's ability to tolerate higher irradiation doses.

Last, although our work is helping reveal some of the fundamental mechanism of microstructural evolution in irradiated nanocrystalline systems, several outstanding questions remain, including the following:

1. Once DZ collapse takes place and the network forms, can the DZ establish itself again by self-healing processes in the GB? In that case, what happens to the loop network?

2. How do the processes in the interior of the grain inform the dynamics of DZ collapse/network formation?

3. Here, we have studied what takes place in a specific GB, but how is the formation/evolution of the network affected by other GBs in the same grain or in the other side of the same GB?

4. What controls the thickness of the network that can form? What is the extent of the region near the GB that can sustain the formation of the network. Put differently, can the network grow indefinitely to maintain a high sink efficiency?

Supplementary Materials

This PDF file includes:

Supplementary Text
Figs. S1 and S2
References

REFERENCES AND NOTES

1. G. A. Somorjai, Y. Li, Impact of surface chemistry. *Proc. Natl. Acad. Sci. U.S.A.* **108**, 917–924 (2011).
2. J. K. Nørskov, F. Abild-Pedersen, F. Studt, T. Bligaard, Density functional theory in surface chemistry and catalysis. *Proc. Natl. Acad. Sci. U.S.A.* **108**, 937–943 (2011).
3. S. Sun, H. Li, Z. J. Xu, Impact of surface area in evaluation of catalyst activity. *Joule* **2**, 1024–1027 (2018).
4. M. A. Meyers, A. Mishra, D. J. Benson, Mechanical properties of nanocrystalline materials. *Prog. Mater. Sci.* **51**, 427–556 (2006).
5. P. Marín, A. Hernando, Applications of amorphous and nanocrystalline magnetic materials. *J. Magn. Magn. Mater.* **215–216**, 729–734 (2000).
6. C. S. Witharamage, J. Christudasjustus, J. Smith, W. Gao, R. K. Gupta, Corrosion behavior of an in situ consolidated nanocrystalline Al-V alloy. *npj Mater. Degrad.* **6**, 15 (2022).
7. R. K. Gupta, N. Birbilis, The influence of nanocrystalline structure and processing route on corrosion of stainless steel: A review. *Corros. Sci.* **92**, 1–15 (2015).
8. L. Liu, Y. Li, F. Wang, Electrochemical corrosion behavior of nanocrystalline materials—A review. *J. Mater. Sci. Technol.* **26**, 1–14 (2010).
9. W. Zhang, Y. Xiong, J. Wu, W. Cheng, C. Du, S. Jin, B. Sun, T. Shen, Comparison of helium ion irradiation resistance between nanocrystalline and coarse grained 304 austenitic stainless steel. *Nucl. Fusion* **62**, 126034 (2022).
10. C. Fan, Z. Shang, T. Niu, J. Li, H. Wang, X. Zhang, Dual beam in situ radiation studies of nanocrystalline Cu. *Materials* **12**, (2019).
11. C. M. Barr, N. Li, B. L. Boyce, K. Hattar, Examining the influence of grain size on radiation tolerance in the nanocrystalline regime. *Appl. Phys. Lett.* **112**, 181903 (2018).
12. I. J. Beyerlein, A. Caro, M. J. Demkowicz, N. A. Mara, A. Misra, B. P. Uberuaga, Radiation damage tolerant nanomaterials. *Mater. Today* **16**, 443–449 (2013).
13. S. Srinivasan, C. Kale, B. C. Hornbuckle, K. A. Darling, M. R. Chancey, E. Hernández-Rivera, Y. Chen, T. R. Koenig, Y. Q. Wang, G. B. Thompson, K. N. Solanki, Radiation tolerance and microstructural changes of nanocrystalline Cu-Ta alloy to high dose self-ion irradiation. *Acta Mater.* **195**, 621–630 (2020).
14. S. Dey, J. W. Drazin, Y. Wang, J. A. Valdez, T. G. Holesinger, B. P. Uberuaga, R. H. R. Castro, Radiation tolerance of nanocrystalline ceramics: Insights from yttria stabilized zirconia. *Sci. Rep.* **5**, 7746 (2015).
15. O. El-Atwani, E. Esquivel, E. Aydogan, E. Martinez, J. K. Baldwin, M. Li, B. P. Uberuaga, S. A. Maloy, Unprecedented irradiation resistance of nanocrystalline tungsten with equiaxed nanocrystalline grains to dislocation loop accumulation. *Acta Mater.* **165**, 118–128 (2019).
16. J. E. Nathaniel, P. K. Suri, E. M. Hopkins, J. Wen, P. Baldo, M. Kirk, M. L. Taheri, Grain boundary strain as a determinant of localized sink efficiency. *Acta Mater.* **226**, 117624 (2022).
17. C. M. Barr, E. Y. Chen, J. E. Nathaniel, P. Lu, D. P. Adams, R. Dingreville, B. L. Boyce, K. Hattar, D. L. Medlin, Irradiation-induced grain boundary facet motion: In situ observations and atomic-scale mechanisms. *Sci. Adv.* **8**, 23 (2022).
18. Y. Piao, K. C. Le, Thermodynamic theory of dislocation/grain boundary interaction. *Contin. Mech. Thermodyn.* **34**, 763–780 (2022).
19. C. Y. Hung, G. Vetterick, E. Hopkins, J. K. Balwin, P. Baldo, M. A. Kirk, A. Misra, M. L. Taheri, Insight into defect cluster annihilation at grain boundaries in an irradiated nanocrystalline iron. *J. Nucl. Mater.* **566**, 153761 (2022).
20. O. El-Atwani, A. K. Barnett, E. Martinez, J. Han, A. C. Leff, C.-Y. Hung, J. E. Nathaniel, S. He, E. H. Mang, L. M. Woryk, K. Hattar, B. P. Uberuaga, D. J. Srolovitz, M. L. Falk, J. Marian, M. L. Taheri, Grain boundary metastability controls irradiation resistance in nanocrystalline metals. arXiv.2404.10144 (2024).
21. J. Han, V. Vitek, D. J. Srolovitz, Grain-boundary metastability and its statistical properties. *Acta Mater.* **104**, 259–273 (2016).
22. M. A. Kirk, M. L. Jenkins, H. Fukushima, The search for interstitial dislocation loops produced in displacement cascades at 20 K in copper. *J. Nucl. Mater.* **276**, 50–58 (2000).
23. A. V. Barashev, S. I. Golubov, R. E. Stoller, Theoretical investigation of microstructure evolution and deformation of zirconium under neutron irradiation. *J. Nucl. Mater.* **461**, 85–94 (2015).
24. D. R. Mason, X. Yi, M. A. Kirk, S. L. Dudarev, Elastic trapping of dislocation loops in cascades in ion-irradiated tungsten foils. *J. Phys. Condens. Matter* **26**, 375701 (2014).
25. L. M. Woryk, S. He, E. M. Hopkins, C.-Y. Hung, J. Han, D. J. Srolovitz, J. Marian, M. L. Taheri, Geometrically necessary dislocation fingerprints of dislocation loop absorption at grain boundaries. *Phys. Rev. Mater.* **6**, 083804 (2022).
26. Y. Li, M. Boleininger, C. Robertson, L. Dupuy, S. L. Dudarev, Diffusion and interaction of prismatic dislocation loops simulated by stochastic discrete dislocation dynamics. *Phys. Rev. Mater.* **3**, 073805 (2019).
27. K. Arakawa, K. Ono, M. Isshiki, K. Mimura, M. Uchikoshi, H. Mori, Observation of the one-dimensional diffusion of nanometer-sized dislocation loops. *Science* **318**, 956–959 (2007).
28. D. Hull, D. J. Bacon, "Elastic properties of dislocations" in *Introduction to Dislocations*, D. Hull, D. J. Bacon, Eds. (Butterworth-Heinemann, ed. 5, 2011), chap. 4, pp. 63–83; www.sciencedirect.com/science/article/pii/B9780080966724000049.
29. N. Gao, Z. W. Yao, G. H. Lu, H. Q. Deng, F. Gao, Mechanisms for <100> interstitial dislocation loops to diffuse in BCC iron. *Nat. Commun.* **12**, 225 (2021).
30. X. Wang, N. Gao, Y. Wang, X. Wu, G. Shu, C. Li, Q. Li, B. Xu, W. Liu, Formation of ⟨100⟩ dislocation loop in bcc-Fe via the ternary loop reaction. *Scr. Mater.* **162**, 204–208 (2019).

31. J. Marian, B. D. Wirth, J. M. Perlado, Mechanism of formation and growth of <100> interstitial loops in ferritic materials. *Phys. Rev. Lett.* **88**, 255507 (2002).
32. K. Arakawa, M. Hatanaka, E. Kuramoto, K. Ono, H. Mori, Changes in the burgers vector of perfect dislocation loops without contact with the external dislocations. *Phys. Rev. Lett.* **96**, 125506 (2006).
33. J. Marian, B. D. Wirth, A. Caro, B. Sadigh, G. R. Odette, J. M. Perlado, T. Diaz de la Rubia, Dynamics of self-interstitial cluster migration in pure α-Fe and Fe-Cu alloys. *Phys. Rev. B* **65**, 144102 (2002).
34. G. Vetterick, J. K. Baldwin, A. Misra, M. L. Taheri, Texture evolution in nanocrystalline iron films deposited using biased magnetron sputtering. *J. Appl. Phys.* **116**, 233503 (2014).
35. O. El-Atwani, J. E. Nathaniel, A. C. Leff, K. Hattar, M. L. Taheri, Direct observation of sink-dependent defect evolution in nanocrystalline iron under irradiation. *Sci. Rep.* **7**, 1836 (2017).
36. O. El-Atwani, J. E. Nathaniel, A. C. Leff, B. R. Muntifering, J. K. Baldwin, K. Hattar, M. L. Taheri, The role of grain size in He bubble formation: Implications for swelling resistance. *J. Nucl. Mater.* **484**, 236–244 (2017).
37. P. Erhart, J. Marian, Calculation of the substitutional fraction of ion-implanted He in an α-Fe target. *J. Nucl. Mater.* **414**, 426–430 (2011).
38. J. Portillo, E. F. Rauch, S. Nicolopoulos, M. Gemmi, D. Bultreys, Precession electron diffraction assisted orientation mapping in the transmission electron microscope. *Mater. Sci. Forum* **644**, 1–7 (2010).
39. E. F. Rauch, J. Portillo, S. Nicolopoulos, D. Bultreys, S. Rouvimov, P. Moeck, Automated nanocrystal orientation and phase mapping in the transmission electron microscope on the basis of precession electron diffraction. *Z. Kristallogr* **225**, 103–109 (2010).
40. A. C. Leff, C. R. Weinberger, M. L. Taheri, Estimation of dislocation density from precession electron diffraction data using the Nye tensor. *Ultramicroscopy* **153**, 9–21 (2015).
41. C. Begau, J. Hua, A. Hartmaier, A novel approach to study dislocation density tensors and lattice rotation patterns in atomistic simulations. *J. Mech. Phys. Solids* **60**, 711–722 (2012).
42. R. Matsutani, S. Onaka, Representation of Nye's Lattice Curvature Tensor by Log Angles. *Mater. Trans.* **60**, 935–938 (2019).
43. J. Marian, S. Fitzgerald, G. Po, "Discrete dislocation dynamics simulations of irradiation hardening in nuclear materials" in *Handbook of Materials Modeling* (Springer, 2020), pp. 2243–2271.
44. Plotly Technologies Inc., Collaborative data science (2015); https://plot.ly.
45. B. D. Wirth, G. R. Odette, D. Maroudas, G. E. Lucas, Dislocation loop structure, energy and mobility of self-interstitial atom clusters in bcc iron. *J. Nucl. Mater.* **276**, 33–40 (2000).
46. M. Hernández-Mayoral, D. Gómez-Briceño, Transmission electron microscopy study on neutron irradiated pure iron and RPV model alloys. *J. Nucl. Mater.* **399**, 146–153 (2010).
47. C. McElfresh, N. Bertin, S. Aubry, J. Marian, Coalescence dynamics of prismatic dislocation loops due to vacancy supersaturation. *Phys. Rev. Mater.* **6**, L100601 (2022).
48. C. McElfresh, N. Bertin, S. Aubry, J. Marian, A parallel discrete dislocation dynamics/kinetic Monte Carlo method to study non-conservative plastic processes. *Comput. Mater. Sci.* **209**, 111332 (2022).
49. D. Foley, G. J. Tucker, Quantifying grain boundary damage tolerance with atomistic simulations. *Model. Simul. Mat. Sci. Eng.* **24**, 075011 (2016).
50. I. J. Beyerlein, M. J. Demkowicz, A. Misra, B. P. Uberuaga, Defect-interface interactions. *Prog. Mater. Sci.* **74**, 125–210 (2015).
51. N. Matsunami, T. Murase, M. Tazawa, S. Ninad, O. Fukuoka, T. Shimura, M. Sataka, Y. Chimi, Analysis of N isotope depth profiles in search for reaction of implanted nitrogen with substrate near Si_3N_4–nitride-film and SiO_2-glass-substrate interface. *Nucl. Instrum. Methods Phys. Res., Sect. B* **249**, 185–188 (2006).
52. C. M. Barr, L. Barnard, J. E. Nathaniel, K. Hattar, K. A. Unocic, I. Szlufarska, D. Morgan, M. L. Taheri, Grain boundary character dependence of radiation-induced segregation in a model Ni–Cr alloy. *J. Mater. Res.* **30**, 1290–1299 (2015).
53. O. El-Atwani, E. Martinez, E. Esquivel, M. Efe, C. Taylor, Y. Q. Wang, B. P. Uberuaga, S. A. Maloy, Does sink efficiency unequivocally characterize how grain boundaries impact radiation damage? *Phys. Rev. Mater.* **2**, 113604 (2018).
54. W. Z. Han, M. J. Demkowicz, E. G. Fu, Y. Q. Wang, A. Misra, Effect of grain boundary character on sink efficiency. *Acta Mater.* **60**, 6341–6351 (2012).
55. F. A. Garner, M. B. Toloczko, B. H. Sencer, Comparison of swelling and irradiation creep behavior of fcc-austenitic and bcc-ferritic/martensitic alloys at high neutron exposure. *J. Nucl. Mater.* **276**, 123–142 (2000).
56. S. Huang, J. Marian, Rates of diffusion controlled reactions for one-dimensionally-moving species in 3D space. *Philos. Mag.* **99**, 2562–2583 (2019).
57. O. V. Ogorodnikova, M. Majerle, J. Čížek, S. Simakov, V. V. Gann, P. Hruška, J. Kameník, J. Pospíšil, M. Štefánik, M. Vinš, Positron annihilation spectroscopy study of radiation-induced defects in W and Fe irradiated with neutrons with different spectra. *Sci. Rep.* **10**, 18898 (2020).
58. J. L. Wardini, C. M. Grigorian, T. J. Rupert, Amorphous complexions alter the tensile failure of nanocrystalline Cu-Zr alloys. *Materialia* **17**, 101134 (2021).
59. V. Turlo, T. J. Rupert, Grain boundary complexions and the strength of nanocrystalline metals: Dislocation emission and propagation. *Acta Mater.* **151**, 100–111 (2018).
60. T. J. Rupert, The role of complexions in metallic nano-grain stability and deformation. *Curr. Opin. Solid State Mater. Sci.* **20**, 257–267 (2016).
61. E. Martínez, J. Marian, A. Arsenlis, M. Victoria, J. M. Perlado, Atomistically informed dislocation dynamics in fcc crystals. *J. Mech. Phys. Solids* **56**, 869–895 (2008).
62. M. Tang, J. Marian, Temperature and high strain rate dependence of tensile deformation behavior in single-crystal iron from dislocation dynamics simulations. *Acta Mater.* **70**, 123–129 (2014).

Acknowledgments

Funding: Use of the IVEM-TANDEM facility at Argonne National Laboratory, a user facility funded by the US Department of Energy Office of Nuclear Energy, operated under contract no. DE-AC0206CH11357 by University of Chicago Argonne LLC. of the Center for Nanoscale Materials, an Office of Science user facility, was supported by the US Department of Energy, Office of Science, Office of Basic Energy Sciences, under contract no. DE-AC02-06CH11357. S.H., E.M.H., A.C.L., X.Z., J.M., and M.L.T. acknowledge funding from the US Department of Energy, Office of Basic Energy Sciences, through contract no. DE-SC0020314. **Author contributions:** S.H. developed the simulation codes, generated all the computational results, participated in writing the manuscript draft, and contributed to the scientific and technical discussions. E.H.M. conducted the experiments, generated the experimental data and images, and reviewed and annotated the manuscript draft. A.C.L. assisted with the experimental data interpretation and contributed to the scientific and technical discussions. X.Z. assisted with code implementation, generation of computational results, and making some of the plots. M.L.T. jointly conceptualized the research, secured funding, assisted with the experimental data interpretation, reviewed and annotated the manuscript draft, and contributed to the scientific and technical discussions. J.M. jointly conceptualized the research, designed the simulation methods, wrote the main manuscript draft, and contributed to the scientific and technical discussions. **Competing interests:** The authors declare that they have no competing interests. **Data and materials availability:** All data needed to evaluate the conclusions in the paper are present in the paper and/or the Supplementary Materials.

Submitted 24 July 2023
Accepted 2 April 2024
Published 3 May 2024
10.1126/sciadv.adj8395